Available online at www.sciencedirect.com
SCIENCE DIRECT®
International Journal of Solids and Structures 41 (2004) 6173–6196
INTERNATIONAL JOURNAL OF SOLIDS and STRUCTURES
www.elsevier.com/locate/ijsolstr

Bounds on the complete stress–strain relation for a crack-weakened rock mass under compressive loads

Xiao-ping Zhou [a,*], Yong-xing Zhang [a], Qiu-ling Ha [b], Ke-shan Zhu [a]

[a] School of Civil Engineering, Chongqing University, Chongqing 400045, China
[b] China Three Gorges Project Development Corp., Yichang 443002, Hubei, PR China

Received 6 April 2004; received in revised form 6 April 2004
Available online 17 June 2004

Abstract

The interactions among multiple parallel sliding cracks in rock materials are examined asymptotically in an explicit and quantitative manner in order to reveal fully their so-called shielding and magnification effects on the complete stress–strain relation. Based on the micromechanical framework and the asymptotic analysis, analytical upper and lower bounds are proposed for the complete stress–strain relation for rock masses containing multiple rows of echelon cracks. The present model studies further influence of both the interaction among crack rows and mutual collinear interaction on the constitutive relation and strength for a crack-weakened rock mass. The closed-form explicit expression for the complete stress–strain relation of rock masses containing echelon cracks subjected to compressive loads is obtained. The complete stress–strain relation includes the stages of linear elasticity, nonlinear hardening, strain softening. The results show that the complete stress–strain relation and the strength of a crack-weakened rock mass depend on the crack interface friction coefficient, the sliding crack spacing, the fracture toughness of rock materials, orientation of cracks, the crack half-length and the crack density parameter.

Keywords: The complete stress–strain relation; Compressive loads; The closed-form explicit expression

1. Introduction

There are a great number of cracks in rock and rock-like materials. Their existence and interaction often lead to high stress concentration and become the source of weakening and failure of rock and rock-like materials.

Efforts have been made to study the mechanism governing degradation and failure of a crack-weakened rock mass under compressive loads. Two main approaches are often used to research the constitutive

* Corresponding author. Tel.: +86-23-6540-5987/86-23-6512-1982; fax: +86-2365126168.
E-mail address: zhouxiaopinga@sina.com (X.-p. Zhou).

0020-7683/$ - see front matter © 2004 Elsevier Ltd. All rights reserved.
doi:10.1016/j.ijsolstr.2004.04.023

relation of a crack-weakened rock mass. The first is the phenomenological approach based on continuum damage mechanics (Hudson and Priest, 1983; Oda, 1984; Kawamoto et al., 1988; Shao et al., 1999), in which the effects of microscopic damage mechanisms on properties of rock masses are reflected by scalar, vector or tensor damage variables. Significant advances have been made in understanding the onset, development, and stabilization of failure around boreholes and tunnels. However, it typically requires extensive testing to determine the relevant constitutive law and parameters as well as the strength and yielding criteria. Since such testing is not always possible in petroleum or mining situations, it has always been desirable to incorporate the simplest possible constitutive relations allowing simulation of at least the onset of instability. The second approach is based on micromechanical damage mechanics, which leads to an improved understanding of the underlying physical process.

In the micromechanical approach, the nucleation, growth and coalescence of microcracks are studied and their influences on mechanical properties are reflected in the constitutive relation in certain ways (Zhou et al., 2004). Up to now, the micromechanical damage models for a crack-weakened rock mass reported in the open literature are mainly limited to the pre-peak nonlinear hardening regime (Steif, 1984; Namet-Nasser and Obata, 1988; Kemeny, 1991; Deng and Nemat-Nasser, 1992a,b; Nemat-Nasser and Deng, 1994; Ravichandran and Subhash, 1995; Basista and Gross, 1998; Li et al., 2000a,b).

To study the mechanical behaviors of a crack-weakened rock mass by the micromechanical approach, several micromechanics-based crack models, such as the cylindrical pore model (Zhang et al., 1990), dislocation pile-up model (Wong, 1990) and the frictional sliding crack model have been proposed. Among these models, the frictional sliding crack model is widely accepted (Steif, 1984; Ashby and Hallam, 1986; Namet-Nasser and Obata, 1988; Kemeny, 1991; Deng and Nemat-Nasser, 1992a,b; Nemat-Nasser and Deng, 1994; Ravichandran and Subhash, 1995; Niu and Wu, 1998; Basista and Gross, 1998; Li et al., 2000a,b; Brencich and Gambarotta, 2001; Zhou et al., 2004).

Some of the studies of rock masses containing multiple cracks are based upon the dilute distribution condition where the interaction among the cracks can be neglected. Under this assumption, the constitutive relation can be given in explicit forms. The schemes that are based on the dilute distribution approximation and which neglect the interaction among cracks are only capable of simulating the actual situation accurately at very low levels of the crack density. On the other hand, if the interaction among cracks is taken into account, a rigorous solution can be sought numerically, but the final numerical results, which may be very accurate, are of limited use. Therefore, one simple way to model rock-like materials containing multiple cracks is to assume that the cracks are arranged in a regular pattern so that some approximate, but accurate analytical expressions can be obtained to estimate the overall behaviors of rock-like materials. In many cases, the crack distribution in the rock mass can often be simplified or normalized to the plane periodical collinear cracks or echelon cracks.

Although various methods have been proposed to predict the constitution relation and the strength of rock masses containing multiple cracks, accuracy of these methods cannot be judged due to a lack of proper bounds. It should be noted that the upper and lower bounds for the overall Young's modulus of bodies containing multiple parallel random cracks were proposed by Wang et al. (2000a,b). But their bounds cannot be used for the case of the complete stress–strain relation of rock masses containing echelon cracks subjected to compressive loads.

In this paper, based on the frictional sliding crack model and the internal variable approach (Basista and Gross, 1998), we attempt to obtain the upper and lower bounds on the complete stress–strain relation of a rock mass containing echelon cracks subjected to compressive loads. For this, the so-called "shielding" and "magnification" interaction effects among the multiple cracks are examined. Through this examination of interaction effects, the upper and lower bounds on the complete stress–strain relation for a crack-weakened rock mass are obtained in concise explicit forms. Although only the two-dimensional problem is considered in this paper, the principle is believed to be equally applicable to the three-dimensional case.

2. Constitutive relation for a crack-weakened rock mass

In a rock material, the frictional sliding on the crack surfaces plays a central role in either inelastic deformation or cracking, sliding causes dilatation by opening the crack at asperities and by inducing local tensile crack at some angle to the crack. Thus, the shear stress on the crack serves as the driving force of inelastic deformation and the material become pressure-sensitive.

The onset of macroscopic inelastic deformation in rock materials is typically attributed to the activation of frictional sliding over the faces of preexisting cracks. During this phase, the only energy dissipating mechanism is the frictional sliding in the shearing mode. The local tensile cracks are induced by the sliding of the initial crack as compressive loads reach a certain critical value. During this phase, the energy is dissipated on the frictional sliding on preexisting flaw and on the growth of wing cracks. During the above two phases, rock materials exhibit nonlinear hardening behavior.

Due to interaction among cracks, some local tensile cracks propagate further in an unstable manner, causing a decrease of capacity of material bearing the compressive loads, inducing behavior of the strain softening of rock materials. During this phase, rock materials exhibit strain softening response.

The total strain increment may be splitted into elastic strain increment part $\mathrm{d}\varepsilon_{ij}^{0}$, which is the strain increment in the intact rock material, and the inelastic strain increment part $\mathrm{d}\varepsilon_{ij}^{m}$, which account for the inelastic deformation of the preexisting cracks and their preferential growth, i.e.

$$\mathrm{d}\varepsilon_{ij} = \mathrm{d}\varepsilon_{ij}^{0} + \mathrm{d}\varepsilon_{ij}^{m} \tag{1}$$

The elastic strain increment is defined by

$$\mathrm{d}\varepsilon_{ij}^{0} = S_{ijkl}^{0}\mathrm{d}\sigma_{kl} \tag{2}$$

where S_{ijkl}^{0} is the elastic compliance tensor of the matrix material.

The inelastic strain increment will be formulated within the thermodynamic framework with internal variables by Rice (1971). The Rice's thermodynamic framework is expressed as

$$\mathrm{d}\varepsilon_{ij}^{m} = \frac{1}{V_0}\sum \frac{\partial f_{\alpha}(\sigma, T)}{\partial \sigma_{ij}}\mathrm{d}\xi_{\alpha} \tag{3}$$

where $f_{\alpha}(\sigma, T)$ is a set of thermodynamic forces conjugated to the internal variable ξ_{α}, σ_{ij} is stress tensor, H represents symbolically the current collection of values of ξ_{α}, V_0 denotes the volume of a representative volume element (RVE), the summation in (3) extends over all sites of the RVE where the microstructural rearrangement takes place.

2.1. The frictional sliding under compression

Consider an infinite plate containing echelon arrays of cracks. Establish the global coordinate system $(o - x_1\ x_2)$ and the local coordinate system $(o_1 - x_1'\ x_2')$, in which x_1'-axis is parallel to the normal vector $\mathbf{n}$, as shown in Fig. 1. The half length of the crack is a, and the angle of local coordinate x_1' against the global coordinate x_1 is θ.

During the phase of the activation of frictional sliding on the faces of the preexisting cracks, influence of the interaction among cracks on the deformation of rock masses can be neglected. The expression for the resolved stresses in the local coordinate system (x_1', x_2') is

$$\begin{cases} \sigma_{22}^{\mathrm{r}} = \sigma_{11}\cos^2\theta + \sigma_{22}\sin^2\theta \\ \tau_{12}^{\mathrm{r}} = \frac{1}{2}(\sigma_{11} - \sigma_{22})\sin^2\theta \end{cases} \tag{4}$$

where σ_{11}, σ_{22} are all positive.

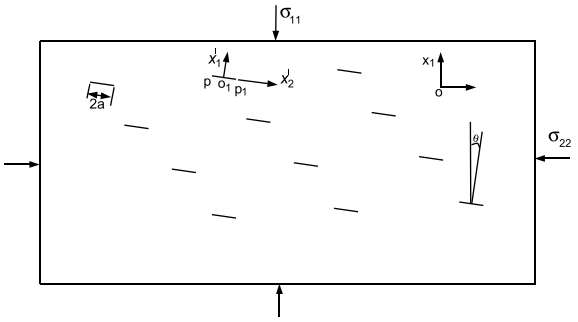

Fig. 1. The mechanical model for rock masses containing multiple rows of echelon cracks subjected to compressive loads.

The effective shear stress that drives the frictional slip on the surface of preexisting cracks can be expressed as

$$\tau_{\text{eff}} = (\sigma_{11} - \sigma_{22})\cos\theta\sin\theta - \tau_{\text{c}} - \mu(\sigma_{22}\sin^2\theta + \sigma_{11}\cos^2\theta) \tag{5}$$

where τ_{c} is the cohesion and μ the coefficient of dry friction.

It can be seen that (5) predicts the onset of sliding when $\tau_{\text{eff}} = 0$.

If $\tau_{\text{eff}} \leqslant 0$, a crack-weakened rock mass exhibits the properties of linear elasticity.

The average slip $\bar{b}_0$ of the points on pp_1 is equal to the average Mode II crack opening displacement induced by τ_{eff}, Hence

$$\bar{b}_0 = \frac{\pi a \tau_{\text{eff}}(1 - v_0^2)}{E_0} \tag{6}$$

where E_0 and v_0 are the Young's modulus and Poisson's ratio of the intact rock material.

The specific complementary energy can be decomposed as

$$\psi(\sigma, H) = \psi^0(\sigma) + \Delta\psi(\sigma, H) \tag{7}$$

where $\psi^0(\sigma) = \frac{1}{2}\sigma_{ij}S^0_{ijkl}\sigma_{kl}$, S^0_{ijkl} is the elastic compliance tensor of the matrix material.

The inelastic part of the specific complementary energy due to frictional sliding is equal to the area average of the work done by the actual shear traction along pp_1 on the slip displacements

$$\Delta\psi(\sigma, H) = \frac{1}{A_0}\int_{-a}^{a}\int_0^{b_0(x'_2)} \tau^{\text{r}}_{12}(\sigma, \bar{b}_0)\mathrm{d}b\mathrm{d}x'_2 \tag{8}$$

where A_0 denotes the area of the representative surface element.

If $b_0(x'_2) = \bar{b}_0$, expression (8) can be rewritten as

$$\Delta\psi(\sigma, \bar{b}_0) = \frac{2a}{A_0}\int_0^{\bar{b}_0} \tau^{\text{r}}_{12}(\sigma, \bar{b}_0)\mathrm{d}\bar{b}_0 \tag{9}$$

The inelastic change of can be computed by

$$\mathrm{d}^{\text{i}}\psi = \frac{\partial(\Delta\psi(\sigma, \bar{b}_0))}{\partial\bar{b}_0} = \frac{2a}{A_0}\tau^{\text{r}}_{12}\mathrm{d}\bar{b}_0 \tag{10}$$

From (3) and (10), the increment of the inelastic strain in this phase takes the following explicit form:

$$\begin{pmatrix} \mathrm{d}\varepsilon_{11}^{m1} \\ \mathrm{d}\varepsilon_{22}^{m1} \end{pmatrix} = \omega_0 \begin{pmatrix} \sin 2\theta \\ -\sin 2\theta \end{pmatrix} \mathrm{d}\tilde{b}_0 \tag{11}$$

where the normalized slip $\tilde{b}_0 = \bar{b}_0/a$, $\omega_0 = Na^2/A_0$ is the initial crack density parameter, N is the number of cracks, A_0 denotes the area of the representative surface element.

2.2. Crack kinking under compression

Under higher compression, however, it has been experimentally observed that some cracks may propagate into the matrix material in a nonself-similar fashion. These kinked cracks tend to line up in the direction paralleled to the axial compression, further they typically grow gradually with increasing axial compression in a stable manner until a certain critical length is attained, at which unstable growth begins and results in ultimate failure of rock masses.

An exact analytical solution of stress field for the curvilinear wing crack configuration has been given by Nemat-Nasser and Horii (1982) in terms of a singular integral equation. As the solution is complicated, Horii and Nemat-Nasser (1986) suggested that the curvilinear wing cracks can be approximated by straight ones, as shown in Fig. 2a. To study the behavior of the sliding crack under compression, the frictional sliding crack proposed by Horii and Nemat-Nasser (1986) is further represented by a tensile crack of qq_1 whose orientation φ is yet to be determined from maximization of K_{I} of a length of $2l$ subjected at its center to a pair of splitting forces $F = 2a\tau_{\mathrm{eff}}$ as shown in Fig. 2b.

Then the K_{I} and K_{II} factors at q and q_1 in the crack configuration depicted in Fig. 2b are given by

$$\begin{cases} K_{\mathrm{I}} = \frac{F\sin\varphi}{\sqrt{\pi(l+l^*)}} - \sqrt{\pi l}[\sigma_{11}\cos^2(\theta+\varphi) + \sigma_{22}\sin^2(\theta+\varphi)] \\ K_{\mathrm{II}} = -\frac{F\cos\varphi}{\sqrt{\pi(l+l^*)}} - \sqrt{\pi l}\left[\frac{1}{2}(\sigma_{11}-\sigma_{22})\sin 2(\theta+\varphi)\right] \end{cases} \tag{12}$$

where $l^* = 0.27a$ was introduced in Horii and Nemat-Nasser (1986) to make K_{I} and K_{II} nonsingular when the tensile crack length is small.

To facilitate analysis, the actual curvilinear wing crack will be further simplified by a straight opened crack growing parallel to the direction of maximum principal compressive stress σ_{11}. these simplifications are necessary in order to make the micromechanical modelling simple enough for engineering use.

The SIFs (12) takes the simpler form

$$\begin{cases} K_{\mathrm{I}} = \frac{F\cos\theta}{\sqrt{\pi l}} - \sigma_{22}\sqrt{\pi l} \\ K_{\mathrm{II}} = -\frac{F\sin\theta}{\sqrt{\pi l}} \end{cases} \tag{13}$$

where $F = 2a\tau_{\mathrm{eff}}$.

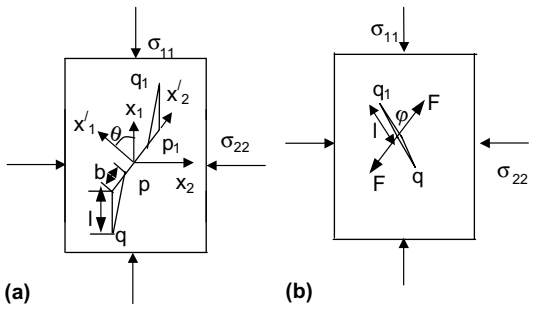

Fig. 2. Frictional sliding crack model with: (a) simplified geometry of tensile wing crack and (b) splitting forces.

The SIFs (12) and (13) are based on the dilute distribution condition where the interaction among the cracks is neglected. For curvilinear winged cracks, the interaction among cracks can be solved only numerically. However, if the approximate model with straight wings and a pair of splitting forces is accepted, then the asymptotic analysis can be applicable. To obtain an explicit closed-form expression of constitutive relation for rock masses containing the plane echelon cracks under compressive loads, the asymptotic analysis including the interaction among the crack rows up to a certain degree of accuracy is performed, and the mutual interaction among the collinear sliding cracks is considered in terms of the work by Tada et al. (1973).

The sliding crack spacing is $2w$, the perpendicular distance between two adjacent rows is H, as shown in Figs. 3 and 5.

On the basis of the asymptotic analysis, the interaction among the crack rows for the periodic rectangular array of cracks and for the diamond-shaped array of cracks under unidirectional tension is obtained by Wang et al. (2000a,b). In this paper, we have extended their works to the straight winged cracks with a pair of splitting forces. However, we need to make a simplifying assumption that splitting forces F can be approximated by the stresses due to a constant normal σ_{22}^0 and shear loading, where $\sigma_{22}^0 = \frac{F\cos\theta}{2l}$, $\tau_{12}^0 = \frac{F\sin\theta}{2l}$ are simply the equivalent uniform distributions of F along the length of crack. Experimental observations have suggested that the crack growth is almost mode I (Ashby and Hallam, 1986), then it is assumed that τ_{12}^0 can be neglected (Ashby and Hallam, 1986; Kemeny, 1991; Deng and Nemat-Nasser, 1992a,b; Nemat-Nasser and Deng, 1994; Li et al., 2000a,b; Zhou et al., 2004).

For the periodic rectangular array of sliding cracks depicted in Fig. 4, the interaction among the sliding crack rows can be solved, the constant pseudo-tractions over the crack faces can be obtained as (see Appendix A)

$$\begin{cases} F_{\mathrm{p}} = \left\{1 + 4\sin^2\frac{\pi l}{2w}\mathrm{e}^{-(H/w)\pi}\left[1 + \frac{H}{w}\pi\right]\right\}^{-1}\sigma_{22}^0 = \frac{A_{\mathrm{r}}F\cos\theta}{2l} = F_{\mathrm{pr}}\cos\theta \\ \sigma_{22}^{\mathrm{pr}} = \left\{1 + 4\sin^2\frac{\pi l}{2w}\mathrm{e}^{-(H/w)\pi}\left[1 + \frac{H}{w}\pi\right]\right\}^{-1}\sigma_{22} = A_{\mathrm{r}}\sigma_{22} \end{cases} \tag{14}$$

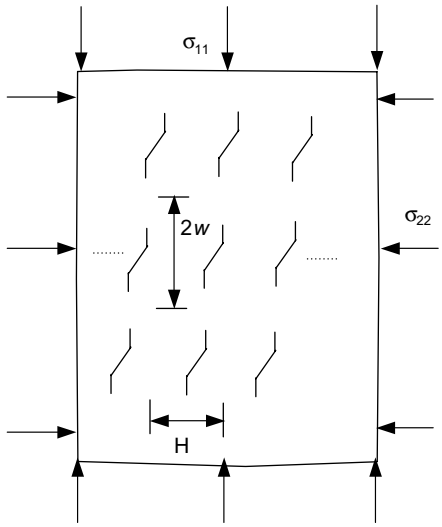

Fig. 3. The doubly periodic rectangular array of sliding cracks.

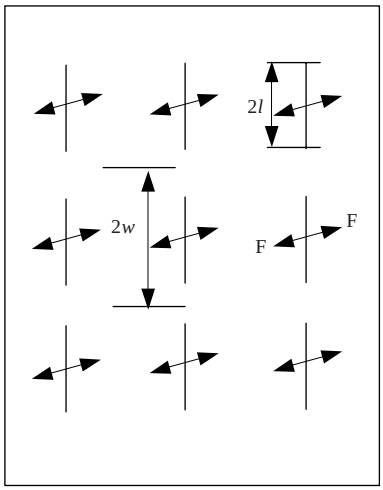

Fig. 4. The equivalent doubly periodic rectangular array of sliding cracks.

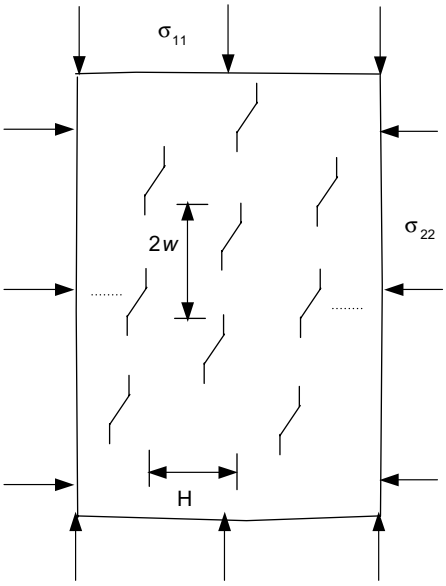

Fig. 5. The diamond-shaped array of sliding cracks.

where

$$F = 2a\tau_{\text{eff}}, A_{\text{r}} = \left\{1 + 4\sin^2\frac{\pi l}{2w}\mathrm{e}^{-(H/w)\pi}\left[1 + \frac{H}{w}\pi\right]\right\}^{-1}, \quad F_{\text{pr}} = \frac{FA_{\text{r}}}{2l}.$$

The constant pseudo-tractions were obtained under the first-order approximation. For $a^2/(2wH) \leqslant 0.25$, the above results are valid. From the analysis of the crack interactions in Appendix B, it is found that the rectangular array will have the strongest shielding effect. The stress intensity factors for mode I at the crack tips for the periodic rectangular array becomes

$$K_{\mathrm{I}} = \frac{F_{\mathrm{pr}} \cos\theta}{\sqrt{w \sin\frac{\pi l}{w}}} - \sigma_{22}^{\mathrm{pr}} \sqrt{2w \tan\frac{\pi l}{2w}} \tag{15}$$

For the diamond-shaped array of cracks depicted in Fig. 6, the constant pseudo-tractions over the crack faces can be written as (see Appendix A)

$$\begin{cases} F_{\mathrm{p}} = \left\{1 - 4\sin^2\frac{\pi l}{2w} \mathrm{e}^{-(H/w)\pi}\left[1 + \frac{H}{w}\pi\right]\right\}^{-1} \sigma_{22}^0 = \frac{A_{\mathrm{d}} F \cos\theta}{2l} = F_{\mathrm{pd}} \cos\theta \\ \sigma_{22}^{\mathrm{pd}} = \left\{1 - 4\sin^2\frac{\pi l}{2w} \mathrm{e}^{-(H/w)\pi}\left[1 + \frac{H}{w}\pi\right]\right\}^{-1} \sigma_{22} = A_{\mathrm{d}} \sigma_{22} \end{cases} \tag{16}$$

where

$$A_{\mathrm{d}} = \left\{1 - 4\sin^2\frac{\pi l}{2w} \mathrm{e}^{-(H/w)\pi}\left[1 + \frac{H}{w}\pi\right]\right\}^{-1}, F_{\mathrm{pd}} = \frac{A_{\mathrm{d}} F}{2l}$$

The constant pseudo-tractions are found to be dependent on geometry of the crack arrays. The above results are valid, provided the crack density parameter $a^2/(2wH) \leqslant 0.58$. If $a^2/(2wH) \geqslant 0.58$, this level of crack density is probably beyond the range of applicability of current asymptotic analysis, and also probably beyond the range of applicability of any existing analytical method. In accordance with the analysis of the crack interactions in Appendix B, it is found that the diamond-shaped array of cracks will have the strongest magnification effect.

The stress intensity factors for mode I at the crack tips for the diamond-shaped array is (see Appendix A)

$$K_{\mathrm{I}} = \frac{F_{\mathrm{pd}} \cos\theta}{\sqrt{w \sin\frac{\pi l}{w}}} - \sigma_{22}^{\mathrm{pd}} \sqrt{2w \tan\frac{\pi l}{2w}} \tag{17}$$

The crack instability condition is

$$K_{\mathrm{I}} = K_{\mathrm{IC}} \tag{18}$$

where K_{I} is the mode I SIF and K_{IC} is the fracture toughness of rock materials.

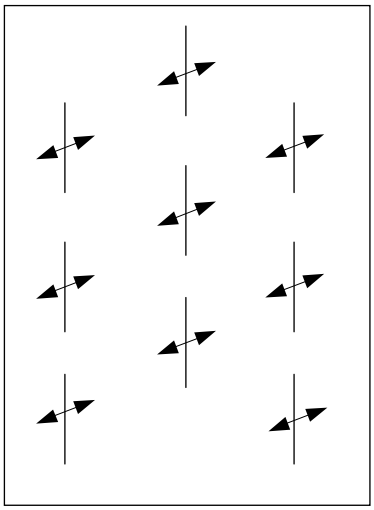

Fig. 6. The equivalent diamond-shaped array of sliding cracks.

For the periodic rectangular array of sliding cracks, the normalized crack length $\tilde{l} = l/a$ can be computed from (15) and (18). Similarly, for the diamond-shaped array of sliding cracks, the normalized crack length can be obtained from (17) and (18).

When the interaction among the crack rows is neglected, due to equilibrium condition in the cross-section qpp_1q_1 and the Mohr–Coulomb condition for the frictional sliding activation of the preexisting crack faces, the effective shear stress that drives the frictional sliding activation on the preexisting crack faces in this phase is obtained by balancing the force along initial slit pp_1 (Zhou et al., 2004):

$$\tau_{\text{eff2}} = \frac{\sqrt{\pi l}}{\sqrt{w \sin \frac{\pi l}{w}}} \tau_{\text{eff}} - \frac{\sqrt{2w \tan \frac{\pi l}{2w}}}{\sqrt{\pi l}} \sigma_{22} \tilde{l} \cos \varphi \tag{19}$$

When the interaction among the crack rows is taken into account, the effective shear stress that drives the frictional sliding activation on the preexisting crack faces in this phase is obtained as

$$\tau_{\text{eff2}} = \frac{\sqrt{\pi l}}{\sqrt{w \sin \frac{\pi l}{w}}} A \tau_{\text{eff}} - \frac{\sqrt{2w \tan \frac{\pi l}{2w}}}{\sqrt{\pi l}} A \sigma_{22} \tilde{l} \cos \varphi \tag{20}$$

where $\tilde{l} = l/a$, $A = A_{\text{d}}$ for the diamond-shaped array of sliding cracks and $A = A_{\text{r}}$ for the periodic rectangular array of sliding cracks.

The average slip $\bar{b}_1$ of points on pp_1 is equal to the average mode II crack opening displacement induced by τ_{eff2}, hence

$$\bar{b}_1 = \frac{1}{2a} \int_{-a}^{a} \frac{4(1-\nu_0^2)\tau_{\text{eff2}}}{E_0} \sqrt{a^2 - x_2'^2} \, \mathrm{d}x_2'^2 = \frac{\pi a \tau_{\text{eff2}} (1-\nu_0^2)}{E_0} \tag{21}$$

When the interaction among the crack rows is neglected, according to Eqs. (19) and (21), the normalized slip $\tilde{b}_1$ is determined by (Zhou et al., 2004)

$$\tilde{b}_1 = \frac{\pi(1-\nu_0^2)}{E_0} \left(\frac{\sqrt{\pi l}}{\sqrt{w \sin \frac{\pi l}{w}}} \tau_{\text{eff}} - \frac{\sqrt{2w \tan \frac{\pi l}{2w}}}{\sqrt{\pi l}} \sigma_{22} \tilde{l} \cos \varphi \right) \tag{22}$$

When the interaction among the crack rows is considered, the normalized slip $\tilde{b}_1$ is determined by

$$\tilde{b}_1 = \frac{\pi A(1-\nu_0^2)}{E_0} \left(\frac{\sqrt{\pi l}}{\sqrt{w \sin \frac{\pi l}{w}}} \tau_{\text{eff}} - \frac{\sqrt{2w \tan \frac{\pi l}{2w}}}{\sqrt{\pi l}} \sigma_{22} \tilde{l} \cos \theta \right) \tag{23}$$

During this phase, the inelastic portion of the specific complementary energy can be written as

$$\Delta\psi(\sigma, H) = \frac{2a}{A_0} \int_0^{\bar{b}_1} \tau'_{12}(\sigma, \bar{b}_1) \mathrm{d}\bar{b}_1 + \frac{2}{A_0} \int_0^{l} G(\sigma, l) \mathrm{d}l \tag{24}$$

where $\tau'_{12} = A\tau^{\text{r}}_{12}\sqrt{\pi l}/\sqrt{w \sin(\pi l/w)} - A\sigma_{22}\tilde{l}\cos\varphi\sqrt{2w\tan(\pi l/2w)}/\sqrt{\pi l}$, $G(\sigma, l) = \frac{(1-\nu_0^2)K_{\text{I}}^2}{E_0}$, $A = A_{\text{d}}$ for the diamond-shaped array of sliding cracks and $A = A_{\text{r}}$ for the periodic rectangular array of sliding cracks.

The inelastic change of $\psi(\sigma, H)$ can be defined as

$$\mathrm{d}^{\text{i}}\psi = \frac{\partial(\Delta\psi)}{\partial\bar{b}_1} \mathrm{d}\bar{b}_1 + \frac{\partial(\Delta\psi)}{\partial l} \mathrm{d}l = \frac{1}{A_0} [2a\tau'_{12} \mathrm{d}\bar{b}_1 + 2G(\sigma, l)\mathrm{d}l] \tag{25}$$

According to Eq. (3), the inelastic part of the strain increment is determined by

$$\begin{pmatrix} \mathrm{d}\varepsilon_{11}^{m2} \\ \mathrm{d}\varepsilon_{22}^{m2} \end{pmatrix} = \frac{\omega_0 A\sqrt{\pi l}}{\sqrt{w\sin(\pi l/w)}} \begin{pmatrix} \sin 2\theta \\ -\sin 2\theta \end{pmatrix} \mathrm{d}\tilde{b}_1 + \frac{8\omega_0\pi(1-v_0^2)\tilde{w}\tan\frac{\pi l}{2w}}{E_0} A^2 \begin{pmatrix} 0 \\ \sigma_{22} \end{pmatrix} \mathrm{d}\tilde{l} + \omega_0 \begin{pmatrix} 0 \\ -2\cos\theta \end{pmatrix} \left(\frac{\sqrt{2w\tan(\pi l/2w)}}{\sqrt{\pi l}} A\tilde{l}\mathrm{d}\tilde{b}_1 + \frac{4(1-v_0^2)\sqrt{2\tan\frac{\pi l}{2w}}}{\sqrt{\sin\frac{\pi l}{w}E_0}} A\tau_{\mathrm{eff1}}\mathrm{d}\tilde{l} \right) \tag{26}$$

where $\tau_{\mathrm{eff1}} = \frac{F_{\mathrm{pd}}}{2a}$ for the diamond-shaped array of sliding cracks, $\tau_{\mathrm{eff1}} = \frac{F_{\mathrm{pr}}}{2a}$ for the periodic rectangular array of sliding cracks, $A = A_{\mathrm{d}}$ for the diamond-shaped array of sliding cracks and $A = A_{\mathrm{r}}$ for the periodic rectangular array of sliding cracks, $\tilde{w} = \frac{w}{a}$.

The strength $\sigma_{11\max}$ and $\sigma_{22\max}$ of rock masses with the diamond-shaped array of sliding cracks can be determined from Eqs. (17) and (18). Similarly, the strength $\sigma_{11\max}$, $\sigma_{22\max}$ of rock masses with the periodic rectangular array of sliding cracks can be determined from Eqs. (15) and (18). The strength of a rock mass with the periodic rectangular array of sliding cracks is obviously higher than that with the diamond-shaped array of sliding cracks.

The inelastic part of the strain increment at the strength failure point can be given by

$$\begin{pmatrix} \mathrm{d}\varepsilon_{11}^{m2} \\ \mathrm{d}\varepsilon_{22}^{m2} \end{pmatrix} = \frac{\omega_0 A\sqrt{\pi l}}{\sqrt{w\sin(\pi l/w)}} \begin{pmatrix} \sin 2\theta \\ -\sin 2\theta \end{pmatrix} \mathrm{d}\tilde{b}_2 + \frac{8\omega_0\pi(1-v_0^2)\tilde{w}\tan\frac{\pi l}{2w}}{E_0} A^2 \begin{pmatrix} 0 \\ \sigma_{22\max} \end{pmatrix} \mathrm{d}\tilde{l} + \omega_0 \begin{pmatrix} 0 \\ -2\cos\theta \end{pmatrix} \left(\frac{\sqrt{2w\tan(\pi l/2w)}}{\sqrt{\pi l}} A\tilde{l}\mathrm{d}\tilde{b}_2 + \frac{4(1-v_0^2)\sqrt{2w\tan\frac{\pi l}{2w}}}{\sqrt{w\sin\frac{\pi l}{w}E_0}} A\tau_{\mathrm{eff1\,max}}\mathrm{d}\tilde{l} \right) \tag{27}$$

where

$$\tilde{b}_2 = \frac{\pi A(1-v_0^2)}{E_0} \left(\frac{\sqrt{\pi l}}{\sqrt{w\sin\frac{\pi l}{w}}} \tau_{\mathrm{eff1\,max}} - \frac{\sqrt{2w\tan\frac{\pi l}{2w}}}{\sqrt{\pi l}} \sigma_{22\max}\tilde{l}\cos\theta \right)$$

$\tilde{w} = \frac{w}{a}$ and $\tau_{\mathrm{eff1\,max}} = \frac{F_{\mathrm{pd\,max}}}{2a}$ for the diamond-shaped array of sliding cracks, $\tau_{\mathrm{eff1\,max}} = \frac{F_{\mathrm{pr\,max}}}{2a}$ for the periodic rectangular array of sliding cracks.

2.3. The stage of strain-softening

Under the condition of strain-controlled loading, a crack-weakened rock mass exhibits the behavior of strain-softening. The behavior of strain-softening is caused by cracks experiencing unstable growth, During the stage of strain-softening, the criterion (18) should be satisfied by cracks experiencing unstable growth. The relation between l and σ_{ij} can be obtained approximately from the criterion (18) of unstable growth of cracks. The formulae of the inelastic portion of the specific complementary energy during the stage of strain-softening have the same form as those during the stage of nonlinear hardening.

The inelastic part of the strain increment during the stage of strain-softening can be expressed as

$$\begin{pmatrix} \mathrm{d}\varepsilon_{11}^{m3} \\ \mathrm{d}\varepsilon_{22}^{m3} \end{pmatrix} = \frac{\omega_0 A\sqrt{\pi l}}{\sqrt{w\sin(\pi l/w)}} \begin{pmatrix} \sin 2\theta \\ -\sin 2\theta \end{pmatrix} \mathrm{d}\tilde{b}_3 + \frac{8\omega_0\pi(1-v_0^2)\tilde{w}\tan\frac{\pi l}{2w}}{E_0} A^2 \begin{pmatrix} 0 \\ \sigma_{22} \end{pmatrix} \mathrm{d}\tilde{l} + \omega_0 \begin{pmatrix} 0 \\ -2\cos\theta \end{pmatrix} \left(\frac{\sqrt{2w\tan(\pi l/2w)}}{\sqrt{\pi l}} A\tilde{l}\mathrm{d}\tilde{b}_3 + \frac{4(1-v_0^2)\sqrt{2w\tan\frac{\pi l}{2w}}}{\sqrt{w\sin\frac{\pi l}{w}E_0}} A\tau_{\mathrm{eff1}}\mathrm{d}\tilde{l} \right) \tag{28}$$

where

$$\tilde{b}_3 = \frac{\pi A(1-v_0^2)}{E_0}\left(\frac{\sqrt{\pi\tilde{l}}}{\sqrt{w\sin\frac{\pi\tilde{l}}{w}}}\tau_{\text{eff1}} - \frac{\sqrt{2w\tan\frac{\pi\tilde{l}}{2w}}}{\sqrt{\pi\tilde{l}}}\sigma_{22}\tilde{l}\cos\theta\right)$$

3. Example predictions for the complete stress–strain relation of rock masses under uniaxial compression

3.1. The complete stress–strain relation of rock masses with the doubly periodic rectangular array of sliding cracks

For the doubly periodic rectangular array of sliding cracks, the dependence of the complete stress–strain relation on the crack interface friction coefficient μ, the sliding crack spacing $2w$, the perpendicular distance between the two adjacent row H and the fracture toughness of rock materials K_{IC} is investigated. In simulations, the parameters $E_0 = 45$ GPa, $v_0 = 0.25$, $\tau_c = 0.49$ MPa.

3.1.1. The dependence of the complete stress–strain relation on the friction coefficient μ

Here, we seek to investigate the effect of friction on the growth direction of interacting tension cracks. Since the effective shear stress that drives the frictional slip on the surface of preexisting cracks, defined in Eq. (5), is decreased as the friction between the surfaces of preexisting cracks is increased, the length of the tension cracks driven by the driving force, $F = 2a\tau_{\text{eff}}$, is decreased at a given load. Numerical predictions (Shen et al., 1995) suggested that the coefficient of friction μ affects the path of wing crack propagation. Their works showed that deviation of the direction of wing cracks from the line of preexisting cracks decreases with the increase of the coefficient of friction μ. The above conclusion agrees with experimental observations (Shen et al., 1995; Wong and Chau, 1998). In other words, the tension cracks curve less toward each other for larger coefficients of friction. In order to make the micromechanical modeling simple enough for engineering, it is assumed that the wing cracks are parallel to the direction of the axial compression. The assumption is an acceptable approximate one (Zhou et al., 2003).

In simulations the parameters $\theta = 60°$, $a/w = 1.25$, $H/w = 1$, and the fracture toughness of rock materials is $K_{\text{IC}} = 0.857$ MPa $\sqrt{m}$. Fig. 7 shows the results for $\mu = 0.6$, 0.9 and 1. It is noted that the predicted compressive strength is sensitive to different values of the crack interface friction coefficient μ, The predicted compressive strength is higher as the crack interface friction coefficient μ is larger. The shapes of the complete stress–strain curves are similar for low-, normal-, and high-strength materials. A high-strength material behaves in a linear fashion to a relatively higher stress level than a low-strength material. The complete stress–strain relation includes the stages of linear elasticity, nonlinear hardening and strain softening.

3.1.2. The dependence of the complete stress–strain relation on a/w

In simulations, the parameters $\theta = 60°$, $K_{\text{IC}} = 0.857$ MPa $\sqrt{\text{m}}$, the crack interface friction coefficient is $\mu = 0.8$, and $a/H = 1$. Fig. 8 shows the results for $a/w = 5/6$, 1.0 and 1.25. It is noted that the predicted compressive strength is sensitive to different values of a/w when the neighboring tips of two collinear sliding cracks are close to each other. The predicted compressive strength decreases with the decrease of the sliding crack spacing $2w$. This implies that a crack-weakened rock mass is more stable as the sliding crack spacing $2w$ is larger. The shapes of the complete stress–strain curves are similar for $a/w = 5/6$, 1.0 and 1.25.

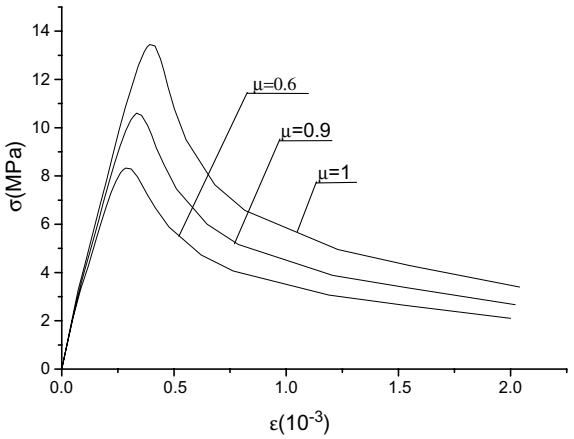

Fig. 7. The dependence of the complete stress–strain relation on the crack interface friction coefficient μ for the doubly periodic rectangular array of sliding cracks.

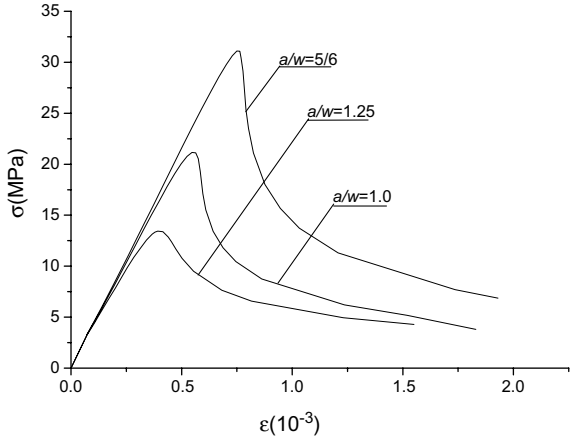

Fig. 8. The dependence of the complete stress–strain relation on a/w for the doubly periodic rectangular array of sliding cracks.

3.1.3. The dependence of the complete stress–strain relation on H/w

In simulations, the parameters $\theta = 60°$, $K_{IC} = 0.857$ MPa $\sqrt{m}$, the crack interface friction coefficient is $\mu = 0.8$, $a/w = 1.25$. Fig. 9 shows the variation of the complete stress–strain curve with the perpendicular distance between the two adjacent row H. It is obvious that the predicted compressive strength is dependent on different values of the perpendicular distance between the two adjacent row when the stacked interaction can not be neglected. The strong shielding effect is associated with interactions among the crack rows. The predicted compressive strength increases with decreasing the perpendicular distance between the two adjacent row H. The above result implies that a crack-weakened rock mass is more stable as the perpendicular distance between the two adjacent row H is smaller. The shapes of the complete stress–strain curves are similar for $H/w = 1$, 2 and 3.

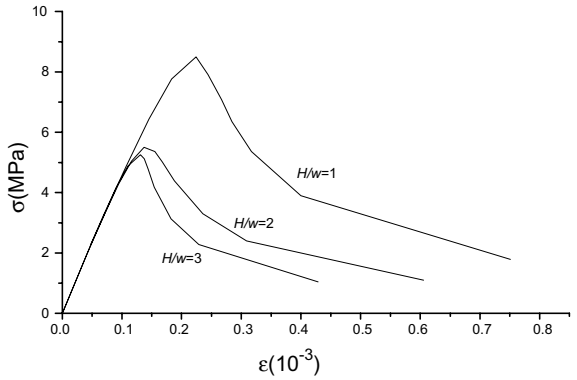

Fig. 9. The dependence of the complete stress–strain relation on H/w for the doubly periodic rectangular array of sliding cracks.

3.1.4. The dependence of the complete stress–strain relation on the fracture toughness of rock materials K_{IC}

In simulations, the parameters $\theta = 60°$, $a/w = 1.25$, $H/w = 1$, and the crack interface friction coefficient is $\mu = 0.8$. Fig. 10 shows the results for $K_{IC} = 0.7$, 0.857 and 1.0 MPa $\sqrt{m}$. It is clear that the predicted compressive strength is sensitive to different values of the fracture toughness K_{IC}. The predicted compressive strength is higher as the fracture toughness of rock materials is larger. The shapes of the complete stress–strain curves are similar for low-, normal-, and high-strength materials. A high-strength material behaves in a linear fashion to a relatively higher stress level than a low-strength material.

3.1.5. The dependence of the complete stress–strain relation on the orientation of cracks θ

In simulations, the parameters τ_c, E_0, v_0 have all been defined previously, $K_{IC} = 0.857$ MPa $\sqrt{m}$, $a/w = 1.25$, $H/w = 1$, and the crack interface friction coefficient is $\mu = 0.8$. Fig. 11 shows that orientation of cracks affects the complete stress–strain relation and the strength for a crack-weakened rock mass.

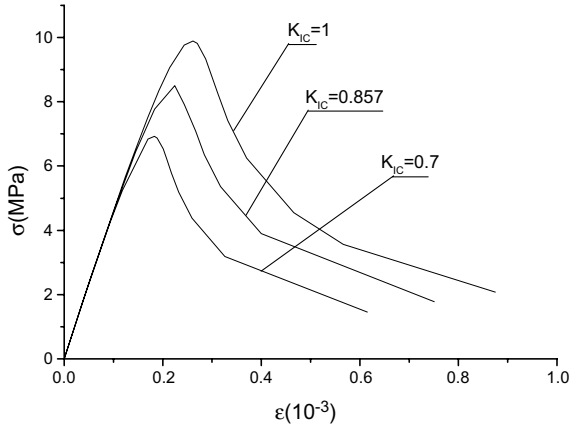

Fig. 10. The dependence of the complete stress–strain relation on the fracture toughness of rock materials for the doubly periodic rectangular array of sliding cracks.

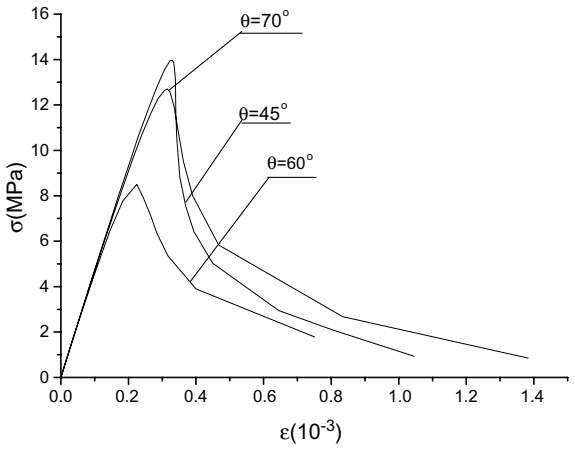

Fig. 11. The dependence of the complete stress–strain relation on θ for the doubly periodic rectangular array of sliding cracks.

3.2. The complete stress–strain relation of rock masses with the diamond-shaped array of sliding cracks

For the diamond-shaped array of sliding cracks, the dependence of the complete stress–strain relation on the crack interface friction coefficient μ, the sliding crack spacing $2w$, the perpendicular distance between the two adjacent row H and the fracture toughness of rock material K_{IC} is investigated. In simulations, the parameters $E_0 = 45$ GPa, $v_0 = 0.25$, $\tau_c = 0.49$ MPa. Compared to the doubly periodic rectangular array of sliding cracks, the strong magnification from diamond-shaped array of sliding cracks results in the lower strength and the larger deformation for a rock mass.

3.2.1. The dependence of the complete stress–strain relation on the friction coefficient μ

In simulations, the parameters E_0, v_0, τ_c have all been defined previously, $\theta = 60°$, $a/w = 1.25$, $H/w = 1$, and the fracture toughness of rock materials is $K_{IC} = 0.857$ MPa $\sqrt{m}$. Fig. 12 shows the results for

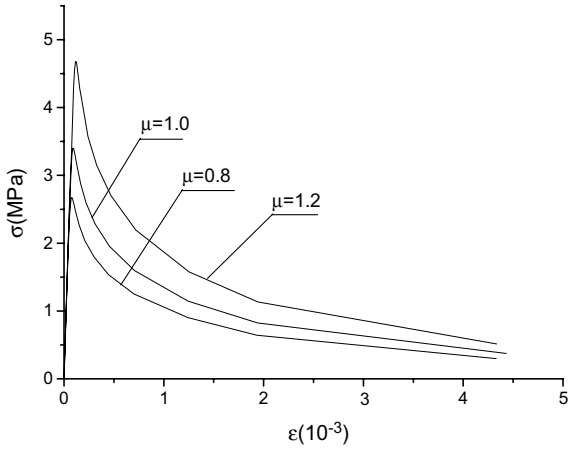

Fig. 12. The dependence of the complete stress–strain relation on the crack interface friction coefficient μ for the diamond-shaped array of sliding cracks.

$\mu = 0.8$, 1 and 1.2. It can be seen that the complete stress–strain curves are dependent on the friction coefficient μ.

3.2.2. The dependence of the complete stress–strain relation on the fracture toughness of rock materials K_{IC}

Fig. 13 shows the results for $K_{IC} = 0.8$ MPa $\sqrt{\text{m}}$ with $\mu = 0.8$, $\theta = 60°$, $H/w = 1$ and $a/w = 1.25$. It is observed from Fig. 13 that the predicted compressive strength is sensitive to different values of the fracture toughness K_{IC}. The predicted compressive strength increases with increasing the fracture toughness of rock materials depicted in Fig. 13.

3.2.3. The dependence of the complete stress–strain relation on H/w

In simulations, the parameters $\mu = 0.8$, $a/w = 1.25$, $K_{IC} = 0.857$ MPa $\sqrt{\text{m}}$ and $\theta = 60°$. Fig. 14 shows the variation of the complete stress–strain curve with H/w. In Fig. 14, when $H/(2w) \leqslant 1$, influence of the interaction among cracks on the strength and deformation is significant. The results are consistent with the works of Wang et al. (2000a,b).

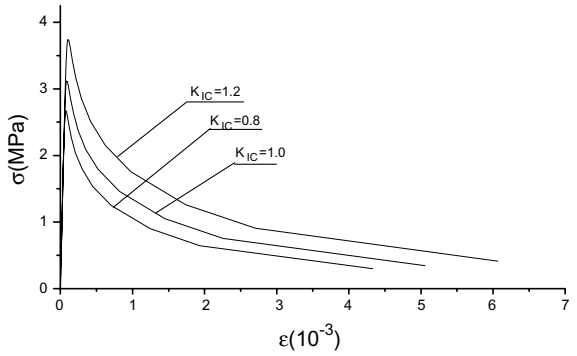

Fig. 13. The dependence of the complete stress–strain relation on the fracture toughness of rock materials for the diamond-shaped array of sliding cracks.

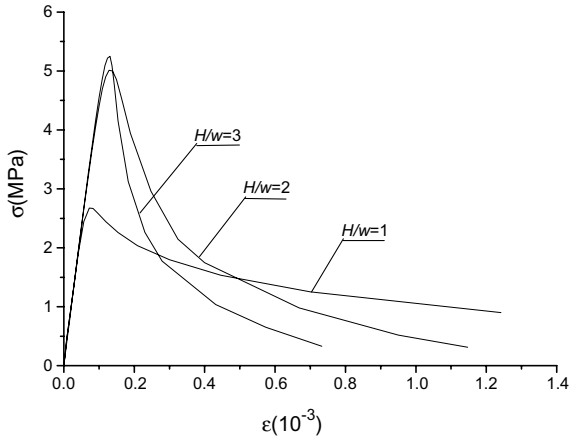

Fig. 14. The dependence of the complete stress–strain relation on H/w for the diamond-shaped array of sliding cracks.

3.2.4. The dependence of the complete stress–strain relation on a/w

Fig. 15 shows the results for $a/w = 1$, 1.25 and 0.65 with $\mu = 0.8$, $K_{IC} = 0.857$ MPa $\sqrt{\text{m}}$, $a/H = 1$ and $\theta = 60°$. It can be seen in Fig. 15 that the peak and residual strength of a rock mass increases with increasing the sliding crack spacing. The shapes of the complete stress–strain curves are sensitive to different values of a/w.

3.2.5. The dependence of the complete stress–strain relation on orientation of cracks θ

In simulations, the parameters E_0, v_0, τ_c have all been defined previously, $a/w = 1.25$, $H/w = 1$, $\mu = 0.8$ and the fracture toughness of rock materials is $K_{IC} = 0.857$ MPa $\sqrt{m}$. Fig. 16 shows the results for $\theta = 45°$, 60° and 70°. It is obvious that the shapes of the complete stress–strain curves are sensitive to different values of orientation of cracks θ.

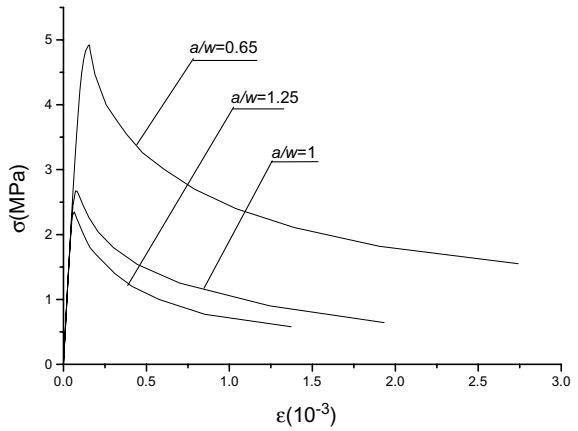

Fig. 15. The dependence of the complete stress–strain relation on a/w for the diamond-shaped array of sliding cracks.

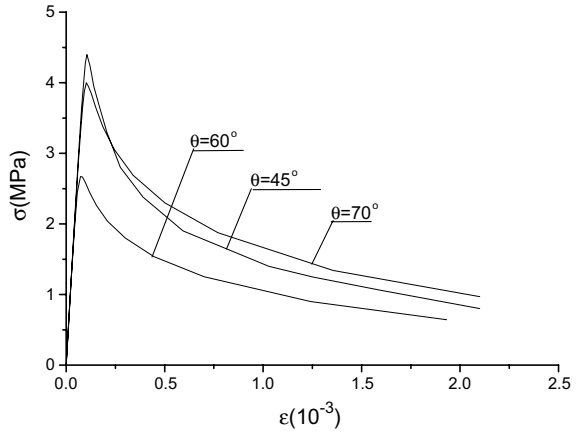

Fig. 16. The dependence of the complete stress–strain relation on θ for the diamond-shaped array of sliding cracks.

4. Example predictions for the strength of a crack-weakened rock mass under uniaxial compression

For the doubly periodic rectangular array of sliding cracks and the diamond-shaped array of sliding cracks, the dependence of the strength on the crack interface friction coefficient μ, the sliding crack spacing $2w$, the perpendicular distance between the two adjacent row H, the fracture toughness of rock materials K_{IC} and orientation of cracks θ is investigated. In simulations, the parameters $E_0 = 45$ GPa, $\nu_0 = 0.25$, $\tau_c = 0.49$ MPa. In Figs. 17 and 18, the strength of a crack-weakened rock mass is plotted against orientation of cracks.

4.1. The dependence of the strength on the friction coefficient μ for the doubly periodic rectangular array of sliding cracks

In simulations, the parameters E_0, ν_0, τ_c have all been defined previously, $a/w = 0.5$, $H/w = 0.2$, and the fracture toughness of rock materials is $K_{IC} = 0.857$ MPa $\sqrt{m}$. Fig. 17 shows the results for $\mu = 0.4$, 0.55 and 0.8. It is clear from Fig. 17 that the strength of a crack-weakened rock mass is sensitive to different values of the crack interface friction coefficient μ and orientation of cracks θ. The strength of a jointed rock mass

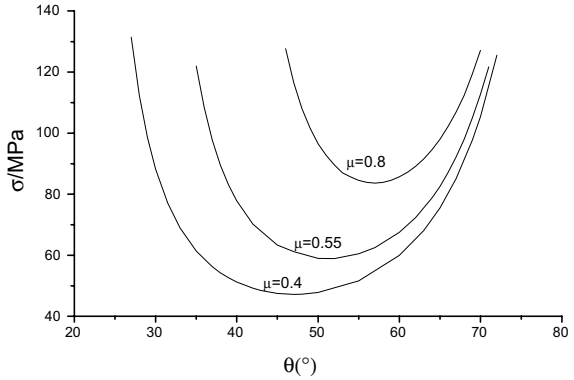

Fig. 17. The dependence of the strength on the friction coefficient μ for the doubly periodic rectangular array of sliding cracks.

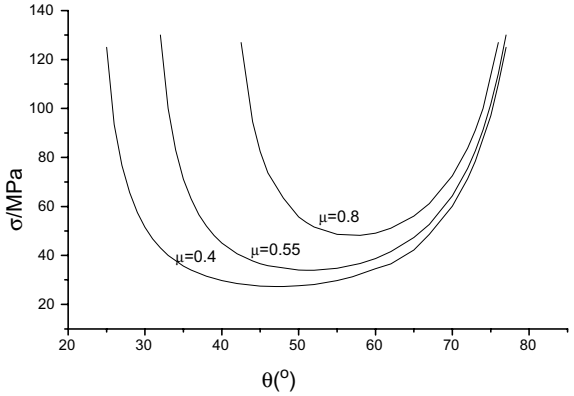

Fig. 18. The dependence of the strength on the friction coefficient μ for the diamond-shaped array of sliding cracks.

increases with increasing the crack interface friction coefficient μ. The strength of a jointed rock mass depends on orientation of cracks.

4.2. The dependence of the strength on the friction coefficient μ for the diamond-shaped array of sliding cracks

In simulations, the parameters $a/w = 1$, $H/w = 1$, and the fracture toughness of rock materials is $K_{IC} = 0.857$ MPa $\sqrt{m}$. Fig. 18 shows the results for $\mu = 0.4$, 0.55 and 0.8. From Fig. 18, it can be observed that the strength of rock masses is sensitive to different values of the crack interface friction coefficient μ and orientation of cracks θ. The strength of a jointed rock mass increases with increase in the crack interface friction coefficient μ. It is found that orientation of cracks affects the strength of a jointed rock mass.

5. Effect of the lateral confinement on interacting tension crack growth

The confining pressure tends to close the wing cracks and at the same time reduce the effective shear stress that drives the frictional slip on the surface of preexisting cracks, defined in Eq. (5). Therefore, the stress intensity factor at the tips of the compression-induced tension cracks is reduced with increasing the lateral confinement. Thus, stress to nucleate the wing cracks is increased by confining pressure, the wing crack length is decreased by the confinement, and the tension crack length reaches the common spacing at a higher applied axial stress, as shown in Figs. 19 and 20. The wing cracks curve less toward each other when confining pressure is increased (Deng and Nemat-Nasser, 1994; Zhou et al., 2003). The analytical results and experimental observations show that axial splitting due to the propagation of a few dominant cracks occurs under uniaxial compressive loads or biaxial compressive loads with low lateral compressive stress, while failure by the formation of a single fault or multiple faults of cracks occurs in the presence of a moderate confinement (Nemat-Nasser and Horii, 1982; Shen et al., 1995; Wong and Chau, 1998; Zhou et al., 2003).

6. Engineering application

To show the application of the complete stress–strain relation for a crack-weakened rock mass, one example is presented here. Underground caverns of the Ertan Hydroelectric Project were constructed in an

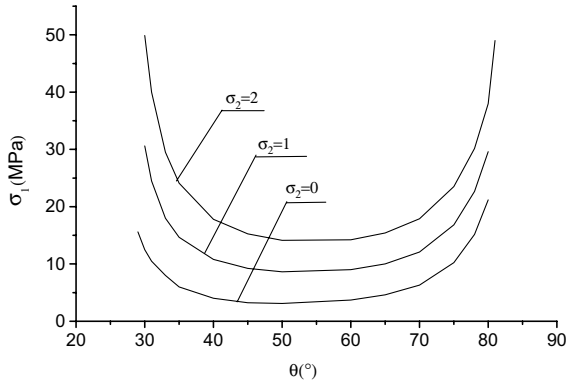

Fig. 19. The dependence of the strength on confining pressure for the diamond-shaped array of sliding cracks when $H = 3$, $a = 5$, $w = 3$, $\mu = 0.5$, $K_{IC} = 0.857$ MPa $\sqrt{m}$.

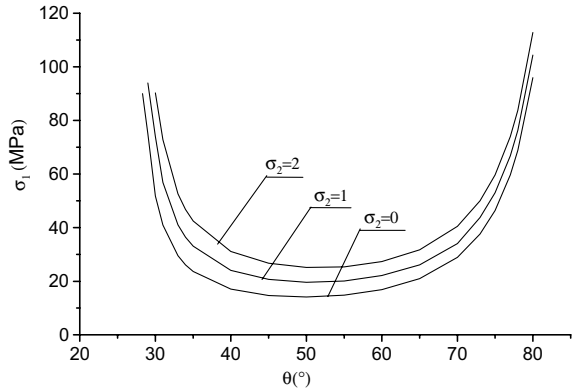

Fig. 20. The dependence of the strength on confining pressure for the doubly periodic rectangular array of sliding cracks when $H = 2$, $a = 5$, $w = 3$, $\mu = 0.5$, $K_{IC} = 0.857$ MPa $\sqrt{m}$.

orthoclase rock mass at the upriver of the Yalong River, Sichuan, China. The orthoclase has a blocky structure, with three main sets of fractures. One set of fractures is dominant. The dominant discontinuities are high in dip and relatively large in size. The structural parameters of the orthoclase were measured in the field by the scan line method and the statistical window method, and their averages are listed in Table 1. The fracture toughness of the orthoclase is $K_{IC} = 0.857$ MPa $\sqrt{m}$. The Young's modulus of the orthoclase is $E_0 = 45$ GPa. The Poisson's ratio of the orthoclase is $v_0 = 0.25$. The uniaxial compressive strength of the orthoclase is 130 MPa. The shapes of the complete stress–strain curves is shown in Fig. 21. It is clear from Fig. 21 that the uniaxial compressive strength of the rock mass is reduced to 27% of the intact rock because

Table 1
Dominant discontinuity data for the orthoclase at underground caverns of the Ertan Hydroelectric Project

Dip direction (°)	Dip angle (°)	Average length ($2a$) (m)	Average spacing (w) (m)	Cohesion (MPa)	Frictional angle (°)	H (m)
150	60	5	2.5	0.49	45	1

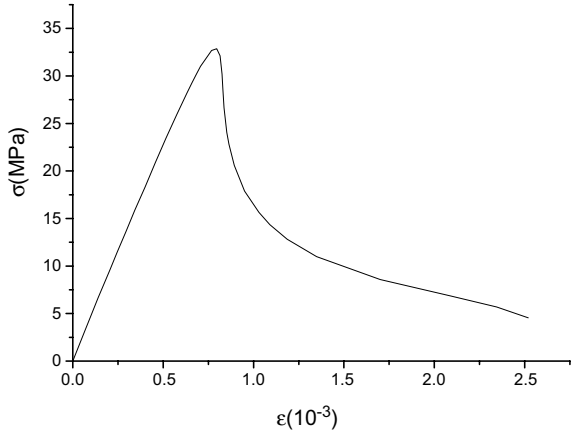

Fig. 21. The complete stress–strain relation of rock masses at underground caverns of the Ertan Hydroelectric Project.

of the existence of cracks. Based on Hoek–Brown criterion, Liu (1993) suggested that the uniaxial compressive strength of the rock mass is 30% of the intact rock. This is in agreement with results obtained by Liu (1993).

7. Discussion and conclusions

In this paper, the two-dimensional frictional sliding crack model has successfully been used to study the constitutive relation of rock masses containing multiple rows of echelon cracks. The model reveals that the nucleation, growth and coalescence of sliding cracks dominate the failure and macroscopic properties of a crack-weakened rock mass under compressive loads.

Several simplifications had been made in the micromechanical modelling. For example, the effect of the coefficient of friction μ on the path of wing crack propagation is not taken into account. This simplification is made primarily to make the micromechanical modeling simple enough for engineering use. In the analysis in Section 2, an asymptotic analysis by Wang et al. (2000a,b) is modified to analyze the interaction of straight winged cracks subjected to a pair of concentrated forces, the closed-form explicit expression for the complete stress–strain relation of a rock mass containing the multiple parallel cracks subjected to compressive loads is obtained.

The sliding crack model is initially a hypothetical model to analyze mechanical properties of brittle materials under compression. With the development of the SEM, it is now revealed that sliding cracks actually exist in brittle materials subjected to compressive loads, and the crack growth results in failure of brittle materials. Hence, it is thought that the sliding crack model can be widely used to study mechanical properties of brittle materials under compressive loads. By using the sliding crack model, the present study reveals that the stress intensity factors and the overall strain depend on the crack configuration, i.e. the periodic rectangular array of sliding cracks and the diamond-shaped array of sliding cracks, and on the microscopic parameters, such as the initial crack length, the crack spacing, orientation of the cracks and the crack density parameter. Finally, the present model is used to analyze the complete stress–strain relation and strength for the jointed rock mass at underground caverns of the Ertan Hydroelectric Project.

Acknowledgements

The authors thank Prof. Charles R. Steele and Prof. Marie-Louise Steele for helpful discussions.

Appendix A

Proof of Eqs. (15) and (17) in Section 2 is derived from the asymptotic analysis by Wang et al. (2000a,b).

For two-dimensional parallel cracks, We need to evaluate collinear and stacked interactions. In order to consider the stacked interaction, we follow the superposition procedure of Karihaloo et al. (1996), and the pseudo-traction technique (Horii and Nemat-Nasser, 1985; Wang et al., 2000a,b), the original problem can be decomposed into a sequence of subsidiary problems in each of which only one row of collinear cracks is considered. In terms of the concept of pseudo-reaction, suppose that the faces of each crack is subjected to a distributed pseudo-traction $\sigma^{\mathrm{p}}_{ij}(x_1)$; $x_1 \in (-l, l)$. By superposition of the subsidiary problems, the traction consistency condition on each crack in a subsidiary problem can be written as

$$\sigma^{\mathrm{p}}_{ij}(x_1) - 2\sum_{j=1}^{+\infty} \int_0^l K_{ijkl}(x_1, x_1^j)\sigma^{\mathrm{p}}_{kl}(x_1^j) = \sigma^0_{ij}, \quad x \in [0, l) \tag{A.1}$$

where $\sigma_{ij}^{\mathrm{p}}(x_1)$ is the pseudo-traction on the crack faces, σ_{ij}^{0} is the applied stress.

Let us now examine the variations of $K_{ijkl}(x_1,x_1^j)$ in order to characterize the crack interactions. Firstly, let the body be subjected to $\sigma_{22}^{o}\neq 0$. Under these loading conditions, we only study the nontrivial component $K_{2222}(x_1,x_1^j)$. The expression for $K_{2222}(x_1,x_1^j)$ was given by Karihaloo and Wang (1997)

$$\begin{aligned}K_{2222}(x_1,x_1^j)=&\frac{2}{w}\mathrm{Re}\left\{\frac{\cos(\pi x_1^j/2w)\sqrt{(\sin(\pi l/2w))^2-(\sin(\pi x_1^j/2w))^2}}{[(\sin(\pi z/2w))^2-(\sin(\pi x_1^j/2w))^2]\sqrt{1-(\sin(\pi l/2w)/\sin(\pi z/2w))^2}}\right\}\\&-\frac{x_2}{w}\mathrm{Im}\left\{\frac{\cos(nx_1^j/2w)\sqrt{(\sin(\pi l/2w))^2-(\sin(\pi x_1^j/2w))^2}}{[(\sin(\pi z/2w))^2-(\sin(\pi x_1^j/2w))^2]^2[1-(\sin(\pi l/2w)/\sin(\pi z/2w))^2]}\right.\\&\times\left[\frac{\pi}{w}\sin\frac{\pi z}{2w}\cos\frac{\pi z}{2w}\sqrt{1-(\sin(\pi l/2w)/\sin(\pi z/2w))^2}\right.\\&\left.\left.+\frac{\pi}{2w}\frac{\sin(\pi l/2w))^2\cos(\pi z/2w)[(\sin(\pi l/2w))^2-(\sin(\pi x_1^j/2w))^2]}{(\sin(\pi z/2w))^3\sqrt{1-(\sin(\pi l/2w)/\sin(\pi z/2w))^2}}\right]\right\}\end{aligned}\tag{A.2}$$

where $z=x_1+ix_2=x_1+i(jH)$, $i=\sqrt{-1}$, $j=1,2,\ldots,+\infty$.

We aim to obtain an approximate closed-form solution of the integral equation (A.1) for the two arrays in Figs. 4 and 6. To this end, we assume that the cracks are so distributed that the higher-order terms (in comparison with terms of order 1) containing $\mathrm{e}^{-(H/2w)\pi}(1\geqslant 4j)$, $\mathrm{e}^{-n(H/2w)\pi}\sin^m(\pi l/2w)$ and $\mathrm{e}^{-n(H/2w)\pi}\sin^m(\pi x_1/2w)$ ($n\geqslant 2j$ and $m\geqslant 2$) can be neglected. The asymptotic expressions for $K_{2222}(x_1,x_1^j)$ for the two arrays of Figs. 4 and 6 are

$$\left\{\begin{array}{c}K_{2222}^{\mathrm{r}}(x_1,x_1^j)\\K_{2222}^{\mathrm{d}}(x_1,x_1^j)\end{array}\right\}=\left\{\begin{array}{c}-2\left[1+2j\frac{H}{2w}\pi\right]\\2\left[1+2j\frac{H}{2w}\pi\right]\end{array}\right\}\frac{2}{w}\mathrm{e}^{-2j(H/w)\pi}\cos\frac{\pi x_1^j}{2w}\sqrt{\sin^2\frac{\pi l}{2w}-\sin^2\frac{\pi x_1^j}{2w}}\tag{A.3}$$

where the superscripts 'r' and 'd' refer to the rectangular and diamond-shaped array, respectively.

Substituting Eq. (A.3) into Eq. (A.1), we have

$$\sigma_{22}^{\mathrm{p}}(x_1)-2\sum_{j=1}^{+\infty}\int_0^l\left\{\begin{array}{c}K_{2222}^{\mathrm{r}}(x_1,x_1^j)\\K_{2222}^{\mathrm{d}}(x_1,x_1^j)\end{array}\right\}\sigma_{22}^{\mathrm{p}}(x_1^j)\mathrm{d}x_1^j=\sigma_{22}^{0}\tag{A.4}$$

As the kernels $K_{2222}^{\mathrm{r}}(x_1,x_1^j)$ and $K_{2222}^{\mathrm{d}}(x_1,x_1^j)$ in Eqs. (A.3) and (A.4) do not contain the variable x_1, the pseudo-tractions $\sigma_{22}^{\mathrm{p}}(x_1)$ which satisfy these equations must be independent of x_1, that is, they must be constant on the crack faces. Thus, $\sigma_{22}^{\mathrm{p}}(x_1)$ are given by

$$\left\{\begin{array}{c}\sigma_{22}^{\mathrm{pr}}\\\sigma_{22}^{\mathrm{pd}}\end{array}\right\}=\left\{\begin{array}{c}A_{\mathrm{r}}\\A_{\mathrm{d}}\end{array}\right\}\sigma_{22}^{0}\tag{A.5}$$

where

$$A_{\mathrm{d}}=\left\{1-4\sin^2\frac{\pi l}{2w}\mathrm{e}^{-(H/w)\pi}\left[1+\frac{H}{w}\pi\right]\right\}^{-1},A_{\mathrm{r}}=\left\{1+4\sin^2\frac{\pi l}{2w}\mathrm{e}^{-(H/w)\pi}\left[1+\frac{H}{w}\pi\right]\right\}^{-1}$$

When the stacked interaction is neglected, following works by Tada et al. (1973), the stress intensity factor of crack array in Figs. 4 and 6 can be written as

$$K_{\mathrm{I}} = \frac{F\cos\theta}{\sqrt{w\sin\frac{\pi l}{w}}} - \sigma_{22}\sqrt{2w\tan\frac{\pi l}{2w}} \tag{A.6}$$

When both the stacked interaction and collinear interaction are taken into account, the stress intensity factor of crack array in Figs. 4 and 6 can be expressed by Eqs. (15) and (17), respectively.

Appendix B

The strongest "magnification" interaction effects and the strongest "shielding" interaction effects for the multiple parallel sliding cracks is proved by using the asymptotic analysis by Wang et al. (2000a,b).

For two-dimensional parallel cracks, we need to evaluate collinear and stacked interactions. Let us suppose that the body contains a row of collinear cracks represented by the solid lines and that a new group of cracks will emerge in the area adjacent to these represented by the broken lines as shown in Fig. 22. The location of one of the newly-emerged cracks is represented by the line segment *CD*. We assume further that the newly-emerged crack is of the same size as the existing cracks. Let us now examine the interaction among the existing collinear cracks and the newly-emerged cracks. For this, we neglect the mutual collinear interactions among the new cracks but concentrate on the interaction among the existing collinear cracks and a single representative new crack, namely, crack *CD*.

Let uniform stress σ^0_{22} be applied on crack surfaces, so that the opening stress $p^{CD}_{ij}(x_1, H)$ at potential location of crack *CD*, which has to be annulled, can be expressed as

$$p^{CD}_{ij}(x_1, H) = T'_{ijkl}(x_1, H)\sigma^0_{kl} \tag{B.1}$$

where the components of $T'_{ijkl}(x_1, H)$ represent the stress components $\sigma_{ij}(x_1, H)$ induced at point (x_1, H) when the body containing the collinear cracks is subjected to uniform stress. Here, for simplicity of analysis,

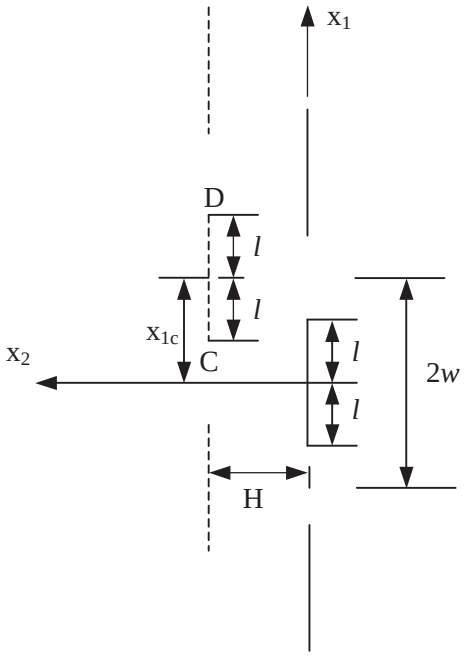

Fig. 22. Interacting cracks. Solid lines represent existing cracks, and dashed lines represent emerging cracks.

we shall ignore the multiple reflection effects of the crack CD and the collinear cracks. Taking the average of $p_{ij}^{CD}(x_1, H)$ over the crack length $2l$, we get

$$\left\langle p_{ij}^{CD}(x_1, H) \right\rangle = T_{ijkl}(x_{1c}, H)\sigma_{kl}^0 \tag{B.2}$$

where x_{1c} is the x_1-coordinate of the center of crack CD, and

$$T_{ijkl}(x_{1c}, H) = \frac{1}{2l}\int_{x_{1c}-l}^{x_{1c}+l} T'_{ijkl}(x_1, H)\mathrm{d}x_1 \tag{B.3}$$

The transformation tensor T_{ijkl} is related to the interaction among the cracks. Therefore, if the configuration of the parallel cracks is such that the magnitude of the transformation tensor T_{ijkl}, or at least the magnitude of some of its major components, is maximized, then the interaction among the cracks will create the maximum increase in deformation of a crack -weakened rock mass. On the other hand, If the configuration of the parallel cracks is such that the magnitude of the transformation tensor T_{ijkl}, or at least the magnitude of some of its major components, is minimized, then the minimum increase in deformation of a crack-weakened rock mass can be expected. These two extreme cases would correspond to the strongest "magnification" interaction effects and the strongest "shielding" interaction effects in the terminology introduced by Kachanov (1992).

Let us now examine the variations of $T_{ijkl}(x_{1c}, H)$ in order to characterize the crack interactions. First, let the body be subjected to $\sigma_{22}^o \neq 0$. Under these loading conditions, we only study the nontrivial component $T_{2222}(x_c, H)$. As $T'_{ijkl}(x_1, H)$ can be obtained in closed form from the formulae in handbook by Tada et al. (1973), $T_{ijkl}(x_{1c}, H)$ can be easily calculated. T'_{ijkl} are equivalent in form and effect to K_{ijkl}. According to Eq. (A.2), it is observed that T_{2222} and T'_{2222} attain their respective maxima at $x_{1c} = w$ and $x_1 = w$, attain their respective minima at $x_{1c} = 0$ and $x_1 = 0$. From the above observations, we can conclude that the crack CD will experience the strongest shielding effect when it is situated immediately above one of the existing collinear cracks and that it will experience the strongest magnification effect when it straddles two existing collinear cracks below it. The effect of a natural configuration of multiple parallel cracks on the complete stress–strain relation of a crack-weakened rock mass should be between these two extreme effects.

References

Ashby, M.F., Hallam, S.D., 1986. The failure of brittle solids containing small cracks under compressive stress states. Acta Metal. Mater. 34, 497–510.

Basista, M., Gross, D., 1998. The sliding crack model of brittle deformation: an internal variable approach. Int. J. Solids Struct. 35 (5–6), 487–509.

Brencich, A., Gambarotta, L., 2001. Isotropic damage model with different tensile–compressive response for brittle materials. Int. J. Solids Struct. 38 (34–35), 5865–5892.

Deng, H., Nemat-Nasser, S., 1992a. Microcrack array in isotropic solids. Mech. Mater. 13, 15–36.

Deng, H., Nemat-Nasser, S., 1992b. Dynamic damage evolution in brittle solids. Mech. Mater. 14, 83–103.

Deng, H., Nemat-Nasser, S., 1994. Microcrack interaction and shear fault failure. Int. J. Damage Mech. 3 (1), 3–37.

Horii, H., Nemat-Nasser, S., 1985. Elastic fields of interacting inhomogeneties. Int. J. Solids Struct. 21, 731–745.

Horii, H., Nemat-Nasser, S., 1986. Brittle failure in compression: splitting, faulting and brittle–ductile transition. Philos. Trans. R. Soc. London 319, 337–374.

Hudson, J.A., Priest, S.D., 1983. Discontinuity frequency in rock masses. Int. J. Rock Min. Sci. Geomech. Abstr. 20 (2), 73–89.

Kachanov, M., 1992. Effective elastic properties of cracked solids: critical review of some basic concepts. Appl. Mech. Rev. 45, 304–335.

Karihaloo, B.L., Wang, J., Grzybowski, M., 1996. Doubly periodic arrays of bridged cracks and short fibre-reinforced cementitious composites. J. Mech. Phys. Solids 44, 1565–1586.

Karihaloo, B.L., Wang, J., 1997. On the solution of doubly periodic array of cracks. Mech. Mater. 26, 209–212.

Kawamoto, T., Ichkawa, Y., Kyoya, T., 1988. Deformation and fracturing behavior of discontinuous rock mass and damage mechanics theory. Int. J. Numer. Methods 12, 1–30.

Kemeny, J.M., 1991. A model for nonlinear rock deformation under compression duo to sub-critical crack growth. Int. J. Rock Mech. Min. Sci. 28 (6), 459–467.

Li, H.B., Zhao, J., Li, T.J., 2000a. Micromechanical modeling of the mechanical properties of a granite under dynamic uniaxial compressive loads. Int. J. Rock Mech. Min. Sci. 37, 923–935.

Li, S., Zhu, W., Chen, W., Xu, J., 2000b. Mechanical model of multi-crack rock mass and its engineering application. Acta Mech. Sin. 16 (4), 357–364.

Liu, D.Y., 1993. Research on mixed mode fracture in rock and strength properties of rock mass with intermittent joints. PhD. Dissertation, Chongqing Jianzhu University, China.

Nemat-Nasser, S., Deng, H., 1994. Strain-rate effect on brittle failure in compression. Acta Metal. Mater. 42 (3), 1013–1024.

Nemat-Nasser, S., Horii, H., 1982. Compression-induced nonplanar crack extension with application to splitting, exfoliation and rockburst. J. Geophys. Res. 87, 6805–6821.

Namet-Nasser, S., Obata, M., 1988. A microcrack model of dilatancy in brittle material. J. Appl. Mech. 52, 24–35.

Niu, J., Wu, M.S., 1998. Analysis of asymmetric kinked cracks of arbitrary size, location and orientation–Part I. Remote Compression. Int. J. Fract. 89, 19–57.

Oda, M., 1984. Similarity rule of crack geometry in statistically homogeneous rock masses. Mech. Mater. 3, 119–129.

Ravichandran, G., Subhash, G.A., 1995. A micromechanical model for high strain rate behaviour of ceramic. Int. J. Solids Struct. 32 (17), 2627–2646.

Rice, J.R., 1971. Inelastic constitutive relations for solids: an internal—variable theory and its application to metal plasticity. J. Mech. Phys. Solids 19, 433–455.

Shao, J.F., Hoxha, D., Bart, M., 1999. Modelling of induced anisotropic damage in granites. Int. J. Rock Mech. Min. Sci. 36, 1001–1012.

Shen, B., Stephansson, O., Einstein, H.H., Ghahreman, B., 1995. Coalesence of fractures under the shear stress experiments. J. Geophys. Res. 100 (6), 5975–5990.

Steif, P.S., 1984. Crack extension under compressive loads. Eng. Fract. Mech. 20, 463–473.

Tada, H., Paris, P.C., Irwin, G.R., 1973. Stress Analysis of Cracks Handbook. Del Research Corporation, St Louis.

Wang, J., Fang, J., Karihaloo, B.L., 2000a. Asymptotics of multiple crack interactions and prediction of effective modulus. Int. J. Solids Struct. 37, 4261–4273.

Wang, J., Fang, J., Karihaloo, B.L., 2000b. Asymptotic bounds on overall moduli of cracked bodies. Int. J. Solids Struct. 37, 6221–6237.

Wong, R.H.C., Chau, K.T., 1998. Crack coalesence in a rock-like material containing two cracks. Int. J. Rock Mech. Min. Sci. 35 (2), 147–164.

Wong, T.F., 1990. A note on the propagation behavior of a crack nucleated by a dislocation pile-up. J. Geophys. Res. 95, 8639–8646.

Zhang, J.X., Wong, T.F., Davis, D.M., 1990. Micromechanics of pressured-induced grain crushing in porous rocks. J. Geophys. Res. 95, 341–351.

Zhou, X.P., Ha, Q., Zhang, Y.X., Zhu, K.S., 2004. Analysis of the deformation localization and the complete stress–strain relation for brittle rock subjected to dynamic compressive loads. Int. J. Rock Mech. Min. Sci. 41 (2), 311–319.

Zhou, X.P., Zhang, Y.X., Zhu, K.S., 2003. Study on the complete stress–strain relation for mesoscopic heterogeneous rock under triaxial compression with moderate or low lateral compressive stress. Chinese J. Geotech. Eng. 25 (5), 606–610.